RSC Applied Interfaces

ROYAL SOCIETY OF CHEMISTRY

PAPER

View Article Online
View Journal | View Issue

Cite this: *RSC Appl. Interfaces*, 2025, **2**, 648

Metal decoration of Si particles *via* high-energy milling for lithium-ion battery anodes†

Khryslyn G. Arañ o,*[a] Beth L. Armstrong,[b] Robert L. Sacci,[a] Matthew S. Chambers,[a] Chun-Sheng Jiang,[c] Joseph Quinn,[d] Harry M. Meyer III,[a] Anton W. Tomich,[e] Amanda Musgrove,[a] Steven Lam,[a] Elena Toups,[a] Chongmin Wang,[d] Christopher S. Johnson[e] and Gabriel M. Veith*[a]

The solid electrolyte interphase (SEI) of silicon (Si) anodes for lithium-ion batteries has been a major focus of research for over a decade. One key factor influencing the formation and composition of the SEI is the desolvation of solvated Li ions, which involves an associated energy barrier. To address this, we aim to disrupt interfacial processes by decorating the Si surface with metals, which are conventionally used to improve the conductivity of Si. This study investigates the preparation and electrochemical performance of metal-decorated Si powders (Si^M, where M represents Ni, Fe, Ti, Ag, Al, or Y) as anode materials, using a simple high-energy ball milling process. STEM reveals that the resulting Si^M architectures either appear as islands on the Si surface or are integrated into the Si bulk, although X-ray diffraction (XRD) confirms that the Si lattice is essentially unchanged. The inherent high electronic conductivity of the metals contributed to lower electrode resistance revealed through scanning spreading resistance microscopy (SSRM), with Si^{Ni} achieving the overall lowest resistance at $\log(R) = 8.7\ \log(\Omega)$, compared to $\log(R) = 10.8\ \log(\Omega)$ for baseline Si, which is also consistent with reduced impedance during cycling. Among the materials studied, Si^{Ni}, Si^{Fe}, and Si^{Ti} demonstrated the most promising performance, reducing overpotential by up to 20 mV, delivering specific capacities above 1000 mAh g^{-1} at a C/3 rate, and exhibiting improved rate capability. Zeta potential measurements suggest that particles with lower zeta potential correlate with better performance. Finally, SEI analysis of insoluble species using XPS revealed that metal decoration, particularly with Ni, results in a stable SEI characterized by lower inorganic LiF content and increased C–O products compared to the baseline Si at high states of charge, consistent with its enhanced performance.

Received 24th November 2024,
Accepted 22nd January 2025

DOI: 10.1039/d4lf00393d

rsc.li/RSCApplInter

Introduction

A range of technologies exists for anode materials in rechargeable batteries. Silicon (Si), in particular, has been extensively studied as a next-generation anode for lithium-ion (Li-ion) batteries due to its exceptionally high theoretical gravimetric capacity of 3579 mAh g^{-1}, which is comparable to that of lithium metal batteries, with a theoretical capacity of 3860 mAh g^{-1}. In addition to lithium, alternative technologies such as sodium-[1–3] and potassium-based[4–6] batteries have also gained attention. However, lithium-based batteries are expected to remain the dominant technology in the foreseeable future. Specifically, Si-containing Li-ion batteries have been a focal point of research, with considerable efforts directed towards their optimization.

Over the last two decades, there has been considerable interest in exploring metal coatings or metal additives for Si anodes.[7–20] This metal doping approach has also been applied to other battery technologies, such as the vanadium molybdenum sulfide (V–Mo–S) system, to address the low conductivity of MoS_2.[21] In Si research, detailed investigations into the use of metal additives have been less extensive compared to other aspects of Si-based technologies. Research efforts have predominantly focused on utilizing metals such as copper (Cu)[8,14,16] and silver (Ag)[7,9,10,15,19,20] due to their

[a] *Chemical Sciences Division, Oak Ridge National Laboratory, Oak Ridge, Tennessee 37831, USA. E-mail: khryslyn.arano@gmail.com, veithgm@ornl.gov*
[b] *Materials Science and Technology Division, Oak Ridge National Laboratory, Oak Ridge, Tennessee 37831, USA*
[c] *Materials Science Center, National Renewable Energy Laboratory, Golden, Colorado 80401, USA*
[d] *Environmental Molecular Sciences Laboratory, Pacific Northwest National Laboratory, Richland, Washington 99354, USA*
[e] *Chemical Sciences and Engineering Division, Argonne National Laboratory, 9700 South Cass Avenue, Argonne, Illinois 60439-4837, USA*

† Electronic supplementary information (ESI) available: Supplementary data to this article can be found online. See DOI: https://doi.org/10.1039/d4lf00393d

superior electrical conductivity, a critical requirement for mitigating the intrinsically low conductivity of Si.[22] Other materials, such as Ni, have also been explored as coatings and/or additives for Si electrodes.[12,18] Among these metals, Ag in particular, generally demonstrates good chemical stability because of its low electronegativity (1.98) that makes it less likely to participate in chemical reactions, which is important in minimizing side reactions.

Due to the conductivity enhancement imparted by the addition of metals, Si as well as graphite-based[23–26] lithium-ion batteries have demonstrated excellent rate performance, *e.g.* 1930 mAh g^{-1} at 1C (ref. 10) and 640 mAh g^{-1} at 5C.[9] Additionally, surface coating of Si has proven effective in blocking the direct contact between Si and the electrolyte, preventing continuous solvent decomposition.[14] Consequently, the solid electrolyte interphase (SEI) properties are likely to change, potentially leading to a thinner SEI or a different SEI composition. For instance, our parallel research has indicated that Cu-decorated Si, denoted as Si^{Cu}, resulted in a SEI with more C–C groups at a delithiated state as indicated by the higher peak intensity at ~284.8 eV compared to the baseline Si. Conversely, the baseline Si exhibited higher peak intensities for –C–O and $–CO_3$-type species at ~289.8 eV.[27] Moreover, the formation of LiF appears to be favored in the Si^{Cu}-based electrode since the F 1s spectra shows one dominant peak at ~684.8 eV (F–Li) whereas the baseline material has two prominent peaks assigned to LiPO-F and F–Li compounds.[27] Polat *et al.*[16] reported the formation of a stable passive film which resulted in enhanced capacity retention (850 mAh g^{-1} after 30th up to the 100th cycle) and coulombic efficiency (99% after 100 cycles) of Cu-capped Si thin film anode. Furthermore, metals in general possess excellent ductility and mechanical strength, offering a potential solution to alleviate the impacts of Si volume expansion. Yin *et al.*[20] attributed improved capacity retention to higher modulus, strength, and hardness of the electrode using Ag nanoparticle additives. Yoo *et al.*[9] highlighted the highly dispersive Ag-coated Si nanoparticles in aqueous and alcoholic solvents, which explains the significant increase in electrical conductivity of the resulting electrodes.

In our parallel study,[27] we investigated different preparation techniques of Si^{Cu}. Specifically, we compared the effects of high-energy ball milling, solution processing, and physical vapor deposition methods. Our findings revealed a significant reduction in overpotential, *i.e.* 100 mV lower for Si^{Cu}, and improved capacity retention in cells employing milled Si^{Cu} compared to those utilizing PVD-prepared Si^{Cu} and baseline Si. Notably, its scalability renders it suitable for industrial-scale production. In this study, we employed the high-energy milling method to prepare metal-decorated Si particles incorporating nickel (Ni), iron (Fe), titanium (Ti), silver (Ag), aluminum (Al), and yttrium (Y). The quantities of metals added were determined based on achieving metal volumes equivalent to 10 wt% and 5 wt% of the conductive carbon additive typically added in composite anodes.

Experimental section

Decorated Si powder preparation

The metal-coated Si powders were synthesized using the procedure described in our concurrent study for Cu-coated Si,[27] which involves high-energy milling of neat Si with a metal, M (M: Ti, Ni, Fe, Al, Y, Ag) in the presence of propylene carbonate (PC – Beantown Chemical >99%).[28] The metals were titanium powder (100 mesh, 99.4%, Alfa Aesar), iron powder (Alfa Aesar, 99%, −20 mesh), nickel powder (Thermo Scientific, 99.8%, −150 + 200 mesh), yttrium powder (Thermo Scientific, 99.6%, −40 mesh) and silver powder (Thermo Scientific, 99.9%, −325 mesh) and aluminum powder (Beantown Chemical, 99.5%, −325 mesh). Two different concentrations were prepared for each metal-decorated Si, corresponding to the volumes of metal equivalent to 10 wt% and 5 wt% of the carbon conductive additive, denoted in the manuscript as 10% and 5% for simplicity. All milling was done in PC to prevent agglomeration and to passivate the surface.

Zeta potential and particle measurements

The zeta potential and particle size of the metal-decorated Si powders were determined using the NanoBrook 90Plus PALS from Brookhaven Instruments. The experimental procedure is documented in our prior publications.[27–30] Phase analysis light scattering (PALS) mode was utilized for zeta potential measurements, while dynamic light scattering (DLS) was employed for particle size assessments. Each reported value represents the average of 100 cycles for each material.

X-ray photoelectron spectroscopy (XPS)

X-ray photoelectron spectroscopy (XPS) measurements of the Si powders were conducted using a Specs EnviroESCA spectrometer. The spectrometer was operated at 15 kV with an Al Kα monochromatic source (1486.6 eV). The Si powders were introduced into the XPS chamber under ambient conditions. Survey scans were acquired with a pass energy of 100 eV and 1 eV energy steps, while high-resolution scans were carried out using a pass energy of 50 eV and a step energy of 0.1 eV. To correct for charging effects, all spectra were calibrated against the C 1s peak at 284.5 eV. Data analysis was conducted using the SpecsLab Prodigy software from SPECS.[27]

XPS analysis of the cycled electrodes were performed using a Thermo Scientific (Waltham, MA, USA) Model K-Alpha instrument, which utilizes monochromated and microfocused Al Kα X-rays (1486.6 eV). To prevent air exposure, the samples were prepared inside an argon-filled glovebox and then transferred to the XPS instrument using a vacuum transfer holder. A 400 μm X-ray spot size was used for sample analysis to maximize signal strength and achieve an average surface composition over the largest possible area. Survey spectra were acquired using a pass energy of 200 eV, while high-resolution core level spectra were obtained using

a pass energy of 50 eV. Throughout the data collection process, the charge neutralization flood gun was employed to maintain stable analysis conditions. Data acquisition and processing were performed utilizing the Thermo Scientific Avantage XPS software package (v.5.96), incorporating mixed Gaussian/Lorentzian peak shapes and a Shirley/Smart type background model for peak fitting.[27,28]

X-ray diffraction (XRD)

Powder XRD data were collected using a Rigaku SmartLab equipped with Cu radiation (2,1 mixture of $K\alpha_1$:$K\alpha_2$ radiation; λ_1 = 1.54056 Å; λ_2 = 1.54439 Å) and a HyPix detector in Bragg Brentano geometry using a $\theta/2\theta$ range of 10–90°, a scan rate of 1.5° min^{-1} and a step size of 0.01°. Powder samples were loaded onto glass bulk sample holders, and a 10 mm incident slit was utilized.

Rietveld refinements[31] were performed using TOPAS v7 (ref. 32) in order to determine (crystalline) phase composition. The starting structures used in the refinements are given in Table S1.† Cell parameters of each phase were refined with symmetry constraints. Additionally, a single atomic displacement parameter per phase was allowed to refine. Atomic coordinates were not refined. Backgrounds were modelled using 12-fold Chebyshev polynomials and peak shapes were modelled using a single Thompson–Cox–Hastings pseudo-Voigt function. In addition, the crystallite sizes of the metals and Si were examined. To determine the crystallite sizes of the metals used to decorate Si, a double-Voigt function[33] native to TOPAS was employed, which models size-broadening effects to peaks. A modified form of the Scherrer equation is used in this function in order to determine the volume-weighted mean column height, L_{vol}:

$$\beta = \frac{k\lambda}{L_{vol}\cos\theta} \quad (1)$$

where β = full-width at half-maximum (FWHM) k = Scherrer constant (0.89 for cubic systems,), λ is the wavelength of the diffracted radiation and θ is the Bragg angle. Attempts to use this function to approximate the Si crystallite sizes resulted in large errors and, in some cases, larger R_{wp} values. Therefore, this function was not applied to the Si phase. Instead, the Si crystallite sizes were estimated using a single-peak approach (SPA), where a pseudo-Voigt peak is fit against the Si (1 1 1) reflection in order to determine the FWHM, which was then used in eqn (1). A weighted-mean value of λ = 1.541853 Å was used to account for the mixed radiation in the emission profile rather than deconvoluting the two peaks. We have also applied this approach elsewhere.[27,30]

Electrode fabrication

Slurries were prepared using the metal-decorated Si as active material, P84 polyimide (Ensinger Austria) as binder, and C45 carbon black (TIMCAL Super C45) as conductive additive. Prior to the slurry mixing, 10 wt% solution of the P84 in *N*-methyl-2-pyrrolidone (NMP – Beantown chemical, >99%) was prepared separately. The slurry components were loaded in a 20 ml polyethylene bottle with 5 pieces of 5 mm yttria stabilized zirconia (YSZ) beads as milling media. Milling was then performed using a Turbula mixer for 1 hour. The slurry was cast on a 9 μm Copper foil substrate (battery grade) with a 100 μm film applicator. The electrodes were dried at 100 °C on a hot plate to remove the NMP solvent followed by curing at 350 °C at 1 hour under argon atmosphere using a ramp rate of 10 °C min^{-1}. The final electrode composition was 80 wt% Si^M, 10 wt% C45, and 10 wt% P84,[27–30] with active material (Si) loading ranging from approximately 0.7–1.0 mg cm^{-2}. The variations in loading across different materials, Si^M, is a consequence of different slurry viscosities resulting from metal decoration of Si, while maintaining consistent solids loading in all the prepared slurries.

Scanning spreading resistance microscopy (SSRM)

Scanning spreading resistance microscopy (SSRM)[34,35] was employed to measure the resistance of the electrodes. SSRM utilizes the contact mode of atomic force microscopy (AFM), wherein a bias voltage is applied between the probe and the sample while measuring the current through the probe. This technique maps the local resistance beneath the probe in a hemispherical volume with a radius of approximately 50 nm. The AFM (Bruker Dimension Icon and Nanoscope V controller) was set up in an argon-filled glovebox, and a logarithmic scale current amplifier (Bruker SSRM module) with a wide resistance range of 10^3 to 10^{14} Ω is used for resistance measurement. A bias voltage was applied to the sample, while the probe (a diamond-coated Si probe, Bruker DDESP-V2) was floating-grounded. The measured resistance is the sum along the current path. The resistance at the back contact was much smaller than the measured resistance and does not significantly contribute. To minimize the probe/sample contact resistance, the probe was pressed into the sample with a relatively large contact force of ~1 mN, ensuring that the measured resistance is predominantly due to the sample's spreading resistance.[27]

Electrochemical testing

Half-cells were assembled using coin cells (CR2032-Hohsen) in an argon-filled glovebox. The working electrode was the Si (13 mm) and the counter/reference was 14 mm Li metal (0.75 mm thickness, Alfa Aesar). Celgard 2325 was used as the separator. The electrolyte was a 1.2 M lithium hexafluorophosphate ($LiPF_6$) solution in ethylene carbonate and ethyl methyl carbonate (3 : 7 wt), henceforth referred to as Gen 2, +3 wt% fluoroethylene carbonate (FEC). After assembly, all cells rested 4 hours prior to cycling. Cycling was performed in galvanostatic mode using a Biologic potentiostat at room temperature with voltage cutoffs from 50 mV to 1 V for lithiation and delithiation, respectively. Three formation steps were performed at C/20 followed by long-term cycling at C/3. In this study, 1C is based on full charge/discharge of $Li_{15}Si_4$ (equivalent to 3579 mAh g^{-1}).

The full cells were assembled using a non-prelithiated Si matched with a lithium nickel manganese cobalt oxide ($LiNi_{0.8}Mn_{0.1}Co_{0.1}O_2$ or NMC811) cathode with an areal loading of 3.07 mAh cm^{-2}, unless otherwise stated. Leakage current tests were also performed using a full cell configuration. The cathodes were dried at 90 °C overnight under vacuum then transferred inside an argon-filled glovebox for coin cell assembly. Gen 2 + 3 wt% FEC electrolyte was used and a Celgard 2325 served as a separator. The Si||NMC811 full cells were cycled from 3.0 V to 4.1 V three times before performing the voltage hold at 4.1 V for 180 hours. Electrochemical impedance spectroscopy (EIS) was measured using a Biologic VSP potentiostat on the same coin cells described above. We converted the EIS data to distribution of relaxation times (DRT) spectra using the RelaxIS tool.[36,37]

Results and discussion

A parallel work[27] from our group focused on Cu-decoration of Si *via* physical vapor deposition and high-energy milling. The milling method resulted in Si^{Cu} electrodes with lower overpotential, equivalent to 300 mV *vs.* 400 mV for the non-decorated Si electrode, and improved capacity retention (88.6% *vs.* 51.2% for the baseline material). Consequently, we became interested in investigating the influence of other surface-deposited metal dopants, including nickel (Ni), titanium (Ti), iron (Fe), aluminum (Al), yttrium (Y), and silver (Ag) using the same milling method. The metals were selected based on their potential to form alloys with Si (Ni, Fe, Y, Ti), as well as those that do not alloy with Si (Al, Ag), as indicated by Si–M phase diagrams.[38–43] This selection allowed us to investigate whether the alloying behavior would persist following the high-energy milling process. STEM images of the Si particles, presented in Fig. 1, show the metal decoration on the Si surface after milling. Similar to our observation with Si and Cu[27], the metals on Si^{Fe} and Si^{Al} form island-like features on the surface of Si rather than homogeneous alloys. The exact atomic scale mixing is not well understood but does not appear extensive. These metallic particles measure approximately 10 nm for Fe and between 10 nm to 50 nm for Al. Additionally, SiO_2 has also formed on the Si surface. In contrast, a distinct architecture is observed in the case of Si^{Ti}, Si^{Y}, and Si^{Ni}, where the metals appear to be incorporated or alloyed within the Si particles rather than merely decorating the surface. For these materials, no visible SiO_2 formation is detected on the Si surface. Given the almost certain presence of SiO_2 or SiO_x on Si powders, especially when exposed to air, it is possible that a wider coverage of the metals on the Si surface has masked these oxides. We note that the architectures obtained did not necessarily match the phase Si–M diagrams mentioned above. The STEM images in Fig. 1 also reveal the irregular shapes of the Si particles, a characteristic attributed to the milling process. Additionally, the particles are observed to be larger than 100 nm in size, with some potentially reaching dimensions of 200–300 nm.

XPS was employed to analyze the surface chemistry of the metal-decorated Si powders. In Fig. 2, the Si 2p core level spectra of the decorated Si particles are presented alongside those of the corresponding metals, specifically Ni 2p, Fe 2p, Al 2p, Ag 3d, Y 3d, and Ti 2p. Analysis of the Si 2p spectra reveals partial oxidation to SiO_x, indicated by peaks around 102–103 eV, with elemental Si detected at approximately 99 eV. Given the presence of SiO_x on all the metal-decorated powders, the absence of visible SiO_x in the STEM images can be attributed to a small oxide layer confined to the surface. Fig. 2 also illustrates further variations among the decorated particles: while Si^{Al} and Si^{Ag} exhibit both metallic (72.7 eV for Al^0) and oxidized (75.1 eV for Al^{3+}) states post-milling, Si^{Fe}, Si^{Y}, and Si^{Ti} predominantly display complete oxidation, based on the peaks at 710 eV, 159.4 eV, and 457.5 eV, for Fe^{3+}, Y^{3+}, and Ti^{4+}, respectively. Conversely, Ni remains in a metallic state after milling. Furthermore, the presence of distinct Si and SiO_x peaks suggests two possibilities for the metal decoration on the Si surface: non-uniform coverage, with patches of metal interspersed with bare Si regions, or a metal layer less than 10 nm thick, considering the surface

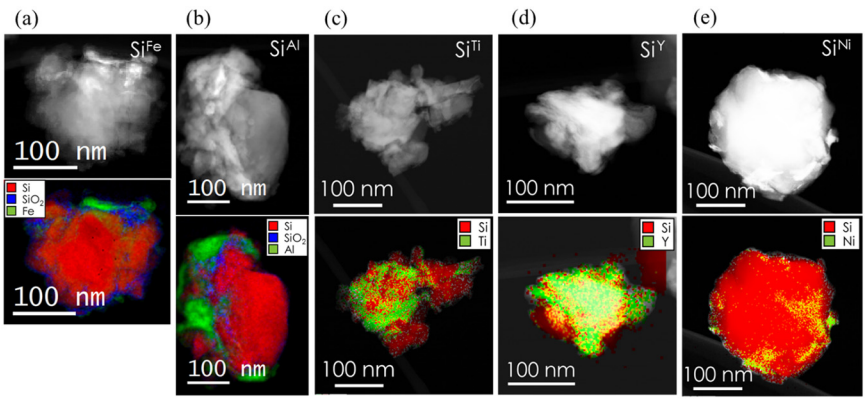

Fig. 1 STEM images and the corresponding electron energy loss spectroscopy (EELS) maps (red corresponds to Si, blue to SiO_2, and green to the metal) of a) Si^{Fe} b) Si^{Al}, c) Si^{Ti} d) Si^{Y}, and e) Si^{Ni} (see Fig. S1a† for Si^{Ag}).

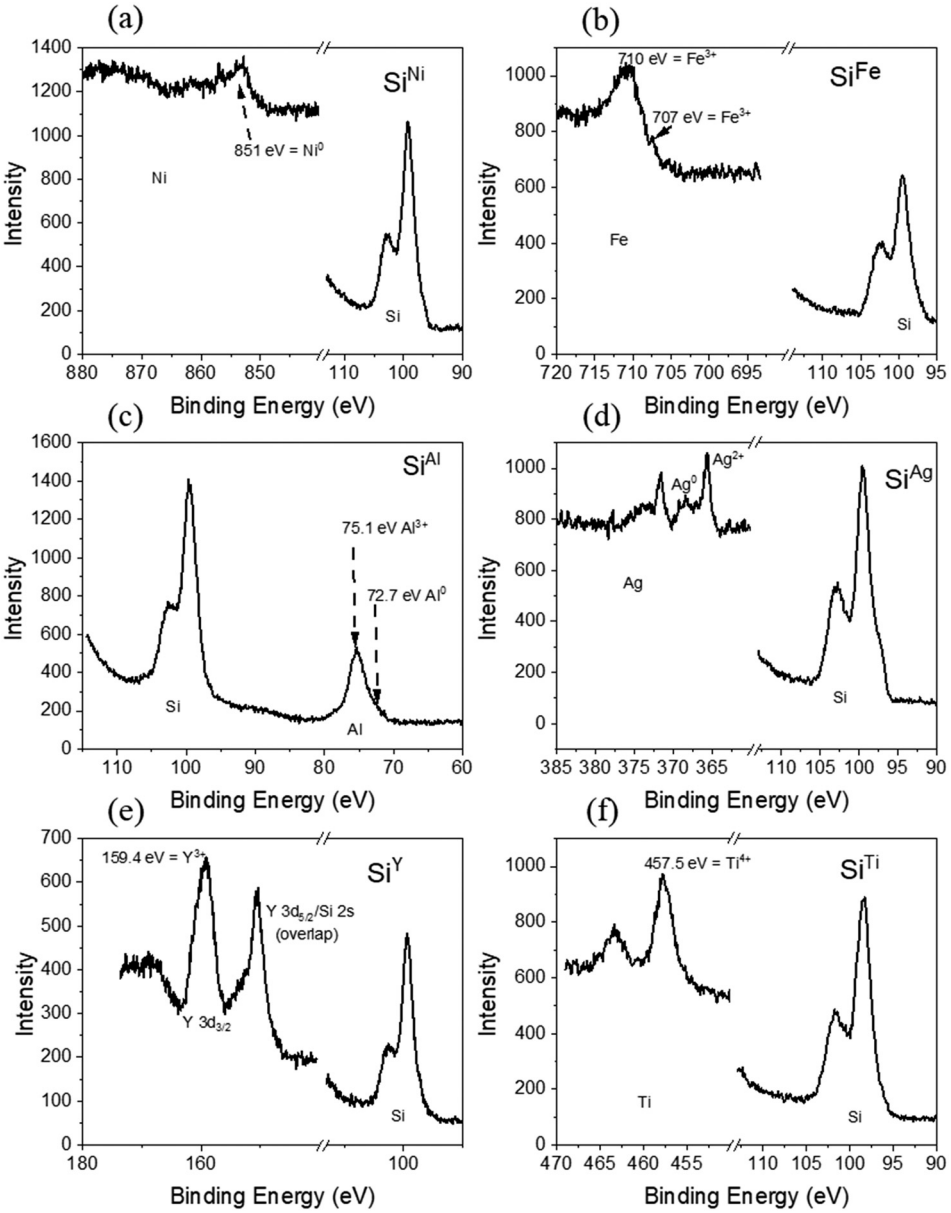

Fig. 2 High-resolution XPS spectra of the metal-decorated Si powders, specifically a) Si^{Ni}, b) Si^{Fe}, c) Si^{Al}, d) Si^{Ag}, e) Si^{Y}, and f) Si^{Ti}. The metal content of the samples is 10% as described in the experimental section.

sensitivity of XPS. The choice of decoration method likely influences these outcomes. For instance, we have found that the milling procedures yields a non-uniform coverage, whereas the PVD method leads to the second case especially at prolonged sputtering times.[27]

In contrast to XPS analysis, which detected oxidation on the surface of all metals except Ni, XRD analysis exclusively indicates the presence of metallic phases. However, this does not rule out the possibility of oxidation. It remains plausible that oxidation has occurred, as suggested by XPS, but the resulting oxide species may be amorphous in nature or confined to the surface. The weight percentages obtained from Rietveld refinement are 70.17(15)% Si and 29.83(15)% Ag for Si^{Ag}, 88.37(15)% Si and 11.63(15)% Al for Si^{Al}, 73.2(2)% and 26.8(2)% Fe for Si^{Fe}, 62.6(2)% and 37.4(2)% Ni for Si^{Ni}, 93.76(16)% and 6.24(16)% Ti for Si^{Ti}, and 97.69(19)% Si and 2.32 (19)% Y for Si^{Y}. The metal amounts in Si^{Ag}, Si^{Al}, Si^{Fe}, and Si^{Ni} are close to the expected values based on the added metal masses during powder synthesis. In contrast, the weight percentages obtained for Si^{Ti} and Si^{Y} are approximately 16% and 20%, respectively, lower than the quantities added during powder preparation, although we note that there are unaccounted peaks in the Si^{Y} XRD pattern and that the Y could be in the unknown phases. This could indicate an inhomogeneous distribution of Ti and Y metal during the milling process, resulting in powders with potentially significantly more (or less) metal than others. The fitting parameters for the reported weight percentages are summarized in Table S2.†

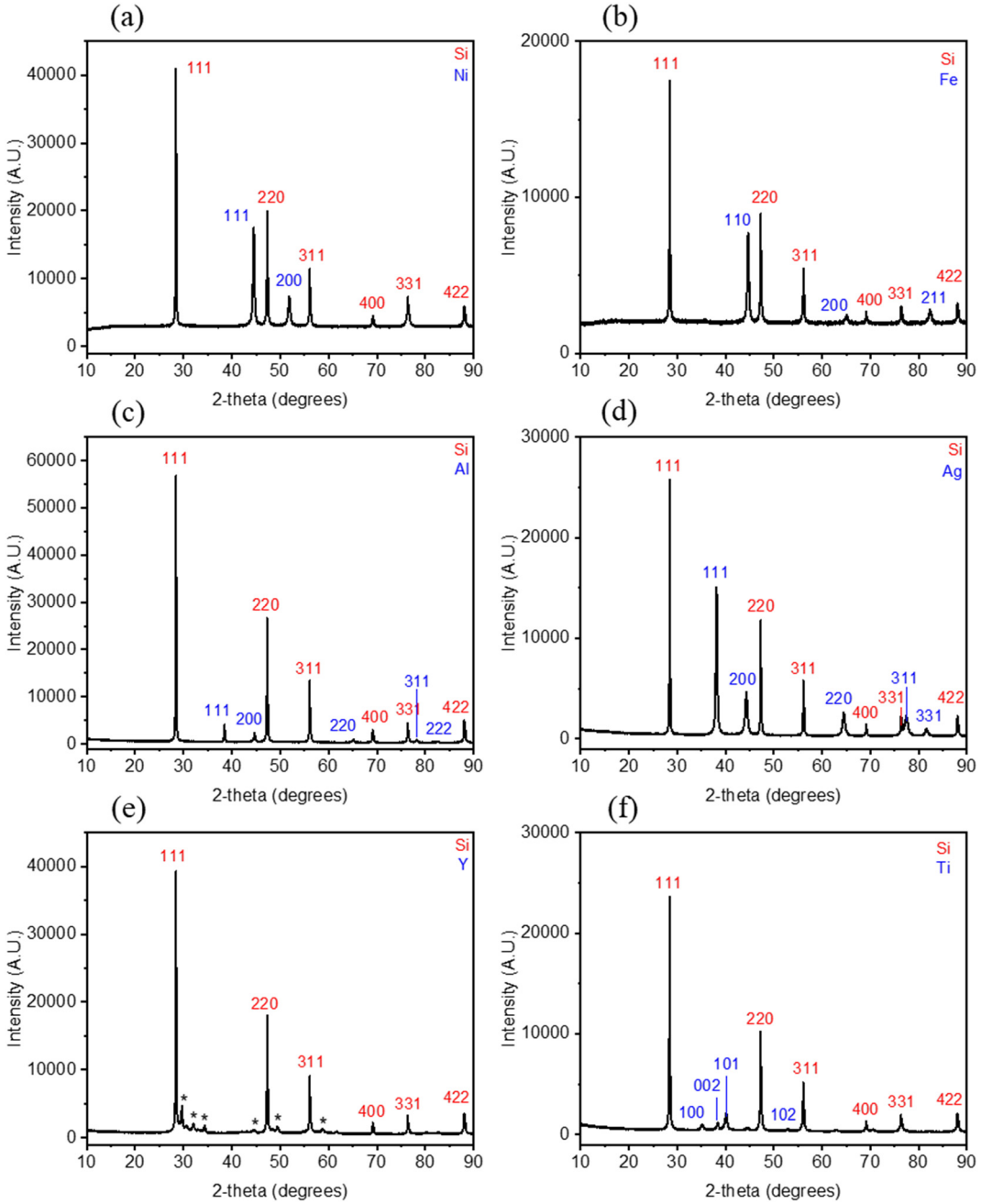

Fig. 3 XRD patterns of a) Si^{Ni}, b) Si^{Fe}, c) Si^{Al}, d) Si^{Ag}, e) Si^{Y}, and f) Si^{Ti} (* Y peaks).

From Fig. 3, the peak positions of all Si diffraction peaks are consistent across all samples. Specifically, the peaks associated with the planes (111), (220), (311), (400), (331), and (442) are all at 2θ angles of 28.4°, 47.3°, 56.1°, 69.1°, 76.4°, and 88.0°. Notably, the peaks align consistently with the non-decorated baseline Si as reported in our parallel work.[27] This consistency indicates that upon metal decoration and regardless of the deposited metal, the Si lattice remains unchanged. It also suggests that the metals are merely decorated onto the surface of the Si rather than integrated or alloyed into its structure. To further verify this, lattice parameters were calculated and summarized in Table S3.† The results show minimal variation in the Si cell parameters across all samples. Specifically, the Si cell parameters for the baseline Si, Si^{Ag}, Si^{Al}, Si^{Fe}, Si^{Ni}, Si^{Ti}, and Si^{Y} are 5.4311(5), 5.4302(3), 5.43059(14), 5.43299(16), 5.4302(3), 5.4330(2), and 5.4299(3), respectively. Additionally, the consistent Si peaks observed across all samples indicate that no new Si-containing phases were formed. This observation rules out one of the hypotheses proposed from the STEM images in Fig. 1, in which the metals appear to be incorporated or alloyed into the Si as in the case for Si^{Ti}, Si^{Y}, and Si^{Ni}.

After synthesizing the metal-decorated powders, particle sizes were measured using the dynamic light scattering method. A general observation is that the decorated Si particles have

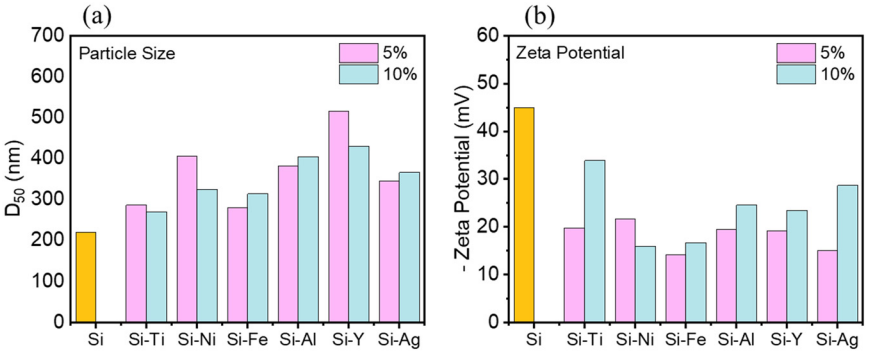

Fig. 4 a) Particle size (D_{50}) of the metal-decorated Si powders measured by dynamic light scattering and their b) zeta potential in NMP solvent measured by phase angle light scattering analysis.

larger particle sizes compared to the baseline material (D_{50} = 220 nm (ref. 28)).[27] As shown in Fig. 4a, the 5% Si^{M} particles exhibit D_{50} values ranging from 287 nm to 517 nm, depending on the metal, M. In comparison, the 10% Si^{M} particles display D_{50} values ranging from 270 nm to 429 nm. As proposed in our parallel work, the larger particle sizes of the decorated Si powders can be attributed to the malleable metals absorbing some of the impact from high-energy ball milling, in addition to the extra material on the Si surface, which, according to STEM images in Fig. 1, can add approximately 10 to 50 nm. Based on this rationale, the 10% samples are expected to exhibit larger particles compared to the 5% samples. However, the opposite trend is observed overall, particularly in the cases of Si^{Ni}, Si^{Ti}, and Si^{Y}. For Si^{Y} and Si^{Ti}, this result aligns with the suggested non-uniform distribution of the metals during the milling process, whereas the reason remains unclear for Si^{Ni}.

Zeta potential measurements were conducted in NMP solvent to assess the suspension stability of the Si powders. The results, presented in Fig. 4b, indicate that the zeta potentials of all the decorated Si powders are of lower magnitudes compared to the non-decorated Si. Specifically, the non-decorated Si has a zeta potential magnitude of 45 mV, while the Si^{M} powders range from 14 mV to 22 mV for the 5% systems and from 16 mV to 29 mV for the 10% systems. The change of zeta potential also supports the presence of metal on the Si surface: a change in the repulsive/attractive distances at the particle surface. Thus, this suggests that the addition of metals can alter the slurry mixing dynamics, potentially leading to more agglomerated slurries. Notably, the 10% systems exhibited higher zeta potential magnitudes than the 5% systems, except for Si^{Ni}.

The SEM-EDX surface images in Fig. 5 offer a detailed look into the morphology of the Si electrodes and elemental distribution of Si particles decorated with various metals within the electrodes. The top row displays SEM micrographs of the electrodes, while the second and third rows show EDX

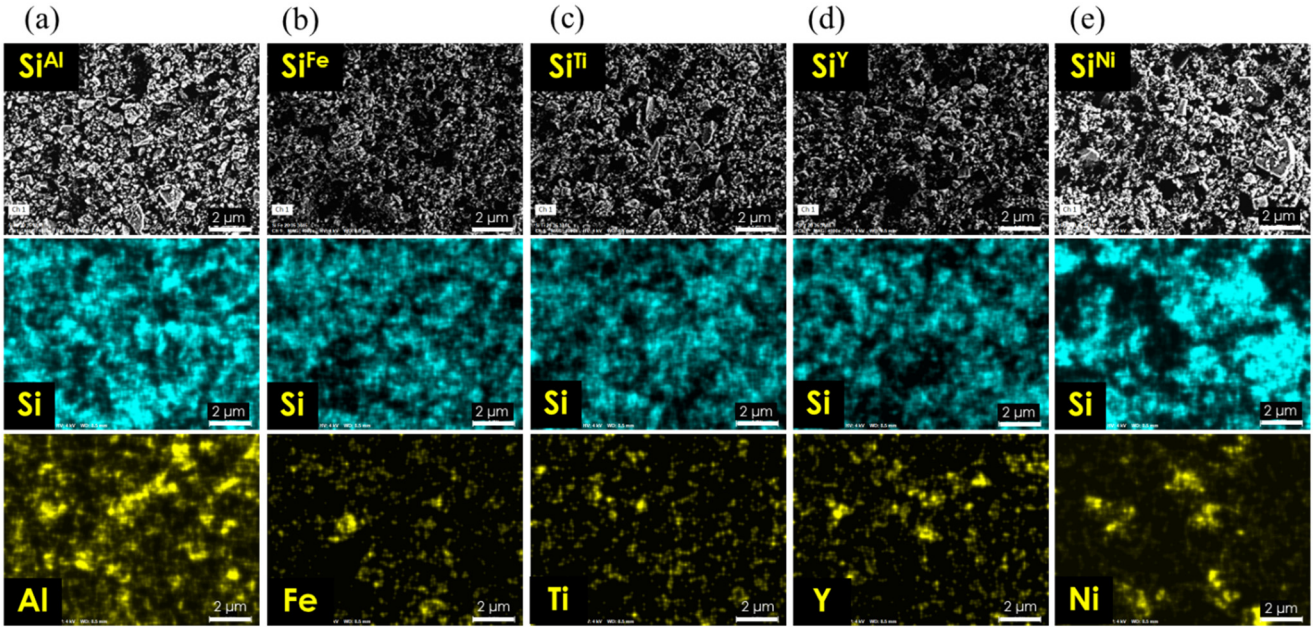

Fig. 5 Surface SEM-EDX images of the decorated Si particles, specifically a) Si^{Al}, b) Si^{Fe}, c) Si^{Ti}, d) Si^{Y}, and e) Si^{Ni} (see Fig. S1b† for Si^{Ag}).

images depicting the distribution of Si and the respective metals. The EDX maps confirm a relatively uniform distribution of Si across all samples, which is crucial for maintaining the base characteristics of the Si particles while enhancing them with metal decoration. The Al distribution appears fairly uniform with some areas of higher concentration, suggesting well-integrated Al within the Si matrix but with some clustering, consistent with the larger Al islands seen in Fig. 1b (bottom row). In contrast, the distributions of Fe, Ti, Y, Ag, and Ni appear more dispersed, indicating good integration with the Si particles, although Y and Ni also exhibit noticeable clustering. These slight differences in metal distribution suggest varying degrees of interaction between the Si and the metal additives.

The SSRM images taken on cross-sections of the electrodes in Fig. 6 show a detailed view of the electrical resistance distribution within the electrodes decorated with Fe and Al. Two areas are shown for each electrode sample. Both Si^{Fe} and Si^{Al} electrodes show regions of high and low resistance, where yellow or brighter regions indicate lower resistance, and blue or darker regions represent higher resistance. In the Si^{Fe} samples, area 1 generally shows lower resistance compared to area 2, highlighting a non-uniform local conductivity across the electrode. Area 2, in particular, exhibits a significant contrast between high and low resistance areas, further suggesting heterogeneous electrode conductivity. The same characteristics can be observed for the Si^{Al} electrode in both area 1 and area 2, where clusters of high- and low-resistance regions exist. Overall, the regions with different resistances can be divided to three categories, high resistance (yellow), medium resistance (pink), and low resistance (blue). While the composite electrode is mixed with carbon, Si, and binder with resistances in the order of carbon $<$ Si $<$ binder, some mild phase separation with materials tendency can be expected. The relative weights of carbon, Si, and binder in the tree types of resistance regions can be in the order of carbon, Si, and binder in the respective yellow, pink, and blue regions of the SSRM images.

In addition to the zoomed-in scans that show details of resistance distributions, we also took SSRM images in large scan areas throughout the electrode thickness on multiple areas for each Si^{M} electrode, to get good statistical resistance values. Fig. S2† shows the overall averaged resistance values measured at different areas of cross-sectioned electrodes. The overall resistance of Si^{Al} is greater than that of Si^{Fe}, with average values of 10.9 logΩ and 9.4 logΩ for Si^{Al} and Si^{Fe}, respectively. Considering all the other metal-decorated Si, the overall resistance from highest to lowest is $Si^{Al} > Si^{Ti} > Si^{Fe} \sim Si^{Ag} \sim Si^{Y} > Si^{Ni}$. The average resistance is 10.0 logΩ for

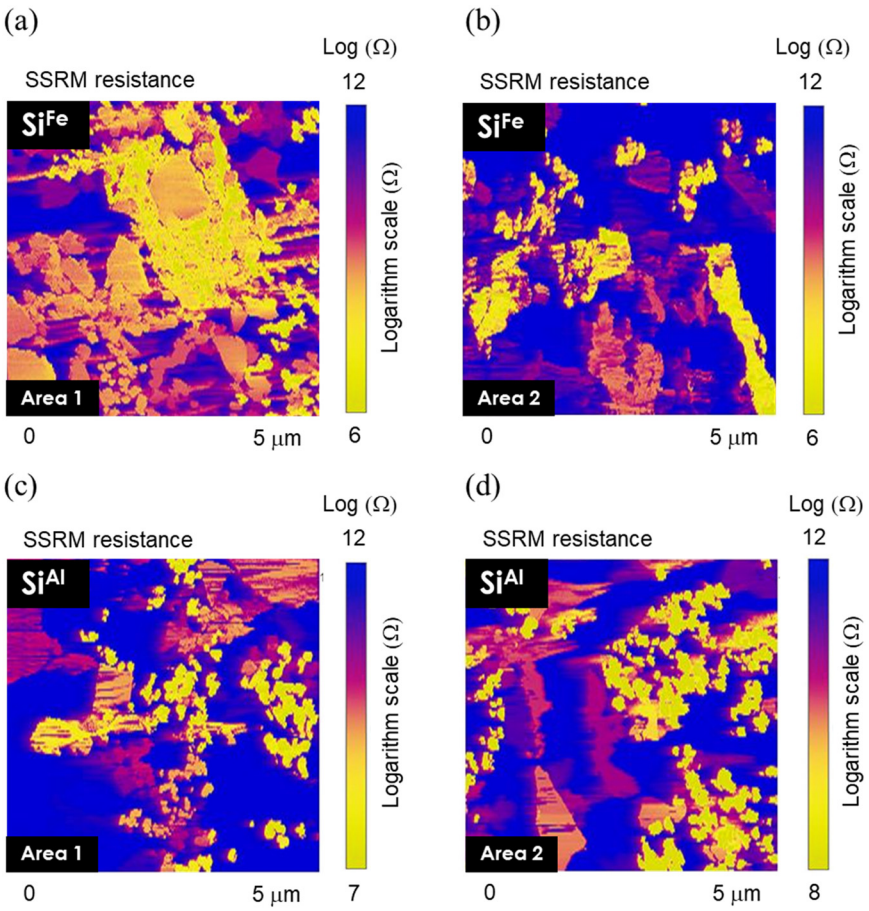

Fig. 6 SSRM resistance images acquired from the cross-section of a and b) Si^{Fe} and c and d) Si^{Al} electrode sample.

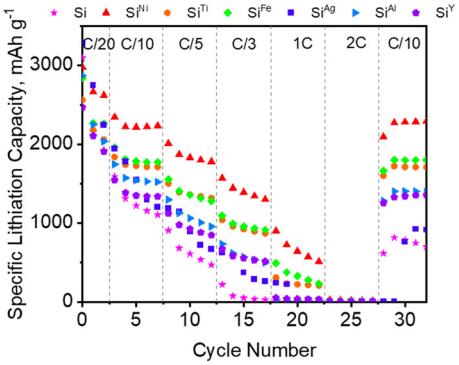

Fig. 7 Half-cell performance of the milled Si^{M} (M: Ni, Ti, Fe, Ag, Al, Y) in Gen 2 + 3 wt% FEC electrolyte at room temperature at different C-rates (1C is based on 3579 mAh g^{-1} for $Li_{15}Si_4$).

Si^{Ti}, 9.6 logΩ for Si^{Ag}, 9.6 logΩ for Si^{Y}, and 8.7 logΩ for Si^{Ni}. It is worth noting that the resistance values for Si^{Ag} and Si^{Y} are highly dispersed, indicating significant heterogeneity in resistance distribution across the electrodes.

Rate tests in half-cell configuration were conducted with 3 cycles at C/20 and 5 cycles each at C/10, C/5, C/3, C, 2C, followed by another 5 cycles at C/10. The results of the half-cell rate performance of Si^{M} (M: Ni, Ti, Fe, Ag, Al, and Y) are depicted in Fig. 7. Notably, the highest specific capacities are achieved with Si^{Ni} across various C-rates ranging from C/20 up to 1C. After the formation at C/20, Si^{Ni} maintains an average of 2245 mAh g^{-1} at C/10, 1856 mAh g^{-1} at C/5, 1406 mAh g^{-1} at C/3, and 667 mAh g^{-1} at 1C. Si^{Ti} and Si^{Fe} also demonstrate decent rate capability. For instance, Si^{Fe} has an average specific capacity of 1880 mAh g^{-1} at C/10, 1380 mAh g^{-1} at C/5, and 976 mAh g^{-1} at C/3. On the other hand, Si^{Ag}, Si^{Al}, and Si^{Y} exhibit rapid capacity decay as the C-rate increases from C/20 to 1C. However, these materials can recover their capacities when the C-rate is reduced to C/10, highlighting that their poor rate behavior is likely a result of transport and/or kinetic limitations, which may be related to electrode conductivity. In addition, their specific capacities remain significantly lower compared to the other Si^{M} systems. The SSRM results support these observations in which Si^{Al} has a higher overall electrode resistance compared to Si^{Fe}. Conversely, Si^{Ni} has the lowest electrode resistance (8.7 logΩ), which also agrees with Ni existing only in metallic state according to XPS, as opposed to the other metals that have partially oxidized. In comparison, the non-decorated baseline Si exhibits considerably lower capacities of least a few hundred mAh g^{-1} lower than the metal-decorated systems. These results underscore the potential of enhancing the rate capability of Si-based electrodes through the incorporation of metallic components in the active material or electrode structure.

Moreover, the rate performance appears to be partially influenced by the zeta potential of the particles. For instance, Ni and Fe, the best-performing systems as discussed above, exhibit the lowest zeta potentials, measuring |16| and |20| mV, respectively. Ti, which also demonstrated good performance, has a zeta potential of |35| mV. In contrast, for the other systems, factors such as electrode resistance and the oxidation state of the metals seem to play a more significant role in determining their overall electrochemical behavior.

The metal-decorated Si electrodes were further cycled in half cells at full capacity (based on 3579 mAh g^{-1} for $Li_{15}Si_4$ alloy) for an extended period at a C/3 rate. Fig. 8 shows the charge–discharge specific capacities of the electrodes from the 20th to 100th cycle, with a 20-cycle interval. Among the

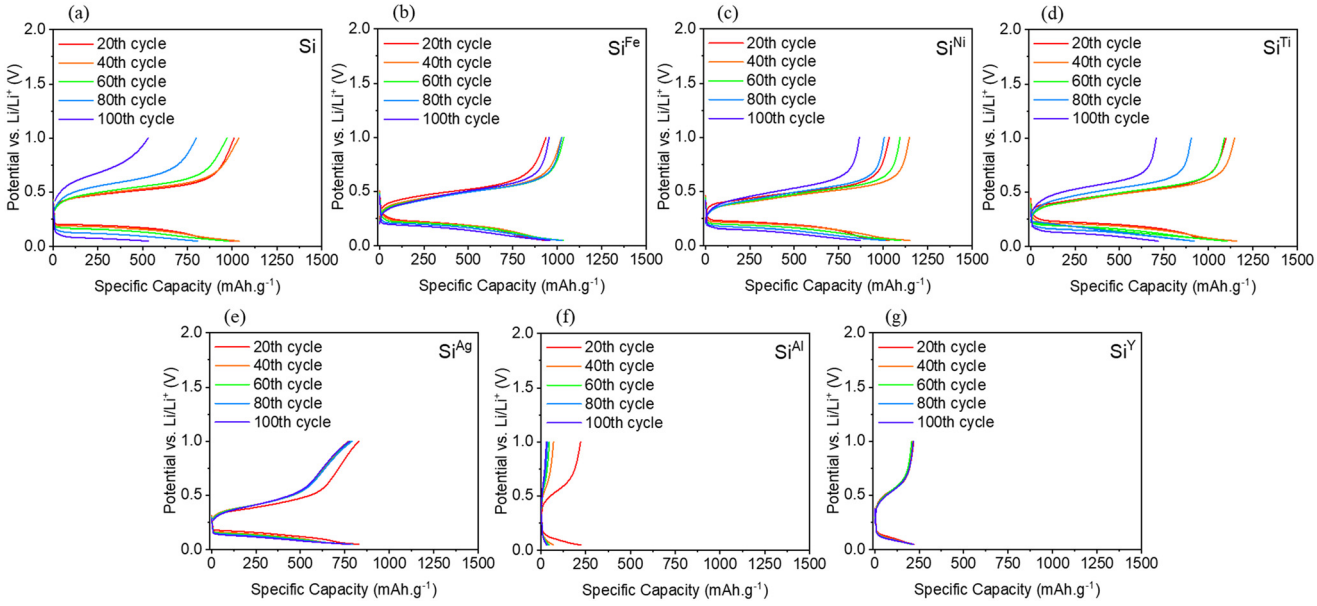

Fig. 8 Half-cell charge–discharge voltage profiles at C/3 (1C based on 3579 mAh g^{-1}) of milled a) Si, b) Si^{Fe}, c) Si^{Ni}, d) Si^{Ti}, e) Si^{Ag}, f) Si^{Al}, and g) Si^{Y} in Gen 2 + 3 wt% FEC at room temperature. The coulombic efficiencies are presented in Table S4.†

six metals investigated, Ni, Ti, and Fe exhibit the highest specific capacities, consistent with the rate test in Fig. 7, reaching just above 1000 mAh g^{-1} after 20 cycles and gradually declining during subsequent cycling. Among these, Si^{Fe} demonstrates the highest capacity retention, maintaining 94.3% of its specific capacity from the 40th to the 100th cycle. Meanwhile, Si^{Ni} and Si^{Ti} exhibit more significant fading, with capacity retentions of 75.9% and 61.9%, respectively. For the baseline Si, the capacity retention is 51.2%.[27] Indeed, an improvement in the cyclability of Si electrodes with metal decoration has been demonstrated, specifically with Cu as we have concurrently reported,[27] Ni, Ti, and Fe from this work. The estimated energy densities of two of the promising systems, Si^{Ni} and Si^{Fe}, are approximately 210 Wh kg^{-1} and 190 Wh kg^{-1}, respectively, compared to the baseline Si, which has an estimated energy density of around 180 Wh kg^{-1}. These values were calculated under a C-rate condition of C/3 and are expected to increase at optimized cycling conditions. Interestingly, the Ag-decorated Si, Si^{Ag}, yields lower specific capacities, delivering only ~830 mAh g^{-1} after the 20th cycle, although losing only an additional 50 mAh g^{-1} by the 100th cycle. Moreoever, the first cycle (Fig. S3†) delivers ~4200 mAh g^{-1} but quickly loses capacity during formation at C/20 and in the initial tens of cycles at C/3. These findings are contrary to prior works on Ag-coated Si (ref. 7, 9, 15, 19, 20) or graphite,[25] which demonstrated improvement in the performance of the electrode with addition of Ag. A possible contributor to the poor performance of Si^{Ag} is the partial oxidation of the Ag particles (XPS) as well as the heterogenous electrode conducvitiy (SSRM).

The behavior of Si^{Al} and Si^{Y} is also particularly interesting. Although both materials can deliver more than 2000 mAh g^{-1} in the first cycle at C/20, similar to Si^{Ag}, they quickly lose capacity upon cycling at a C/3 rate. This rapid capacity loss for Si^{Al} can potentially be linked to its higher overall electrode resistance, as indicated by the SSRM measurements in Fig. 6c and d. The rate tests presented in Fig. 7 support this, showing a steep drop in specific capacities at higher C-rates, which indicate kinetic or transport limitations encountered by these electrodes at higher current densities. Additionally, while it is difficult to obtain an exact value from Fig. 8f, the overpotential of the Si^{Al} cell noticeably increases compared to other electrodes. To aid in this analysis, the differential capacity curves are plotted in Fig. S4.† For instance, from the 1st to the 4th cycle, the lithiation peak for Si^{Al} shifts from 0.24 V to 0.18 V. Si^{Y} exhibits a similar behavior, with higher overpotential as shown in Fig. 8g and a shift in lithiation potential from 0.24 V to 0.19 V (Fig. S4†). In contrast, the other systems show minimal potential shifts. For example, Si^{Ni} and Si^{Fe} only exhibit a slight shift from 0.25 V to 0.24 V over the same cycles. Notably, the electrochemical impedance spectroscopy (EIS) data (Fig. S5†) of all six materials upon cycling from the 3rd (after formation) to the 20th cycle do not indicate any drastic changes in impedance. Specifically, the resistance change does not exceed ~10 Ω for any of the six systems.

A significant finding with metal-decorated electrodes is the observed reduction in overpotential in half-cells, particularly with Si^{Fe}, Si^{Ni}, and Si^{Ti}. Specifically, reductions of ~10 mV were noted for Si^{Fe} and Si^{Ti} and ~20 mV Si^{Ni}, respectively, compared to the baseline Si after the 80th cycle. Additionally, Si^{Cu} exhibited a 100 mV lower overpotential than the baseline Si.[27] Overpotential in Li-ion batteries can be attributed to several factors, including ohmic overpotential, which arises from electronic and ionic resistances within the cell, and kinetic overpotential, which is linked to charge transfer resistance at the electron-ion combination interface. The latter is influenced by changes in lithium concentration within the solid phase, as well as the distribution of lithium ions in the cell. Concentration overpotential, resulting from differences in reactant and product concentrations between the electrolyte and the electrode surface, also contributes to the overall overpotential observed.[44,45] As seen from the characterizations discussed above, the Si^{M} electrodes generally demonstrate a lower overall resistance for the pristine and cycled materials, as discussed subsequent sections. Furthermore, one aspect that is worth exploring is the formation of Li_xSi alloys during lithiation. We postulate that the presence of select metals on Si could lower the energy associated with the formation of LixSi, such as the breaking of Si–Si bonds[46–48] upon Li insertion into the lattice. During the lithiation process, Si and Li undergo several crystalline phase transitions, each with distinct symmetry and size.[49] For instance, the $Li_{15}Si_4$ phase is of particular interest to Li-ion batteries because it is the fully lithiated state of Si at room temperature.[50] However, evidence indicates that Li_xSi also undergo amorphization during cycling.[51] Nonetheless, the breaking of Si–Si bonds remains a critical step for Li to form alloys with Si to begin with, a process associated with surface energy for surface creation, *i.e.* the breaking of bonds.[52] Generally, stronger bonds require more energy to form surfaces. First principles studies[47,52,53] have shown that lithiation weakens the Si–Si bond, destabilizing the Si network and leading to the formation of Li_xSi phases mentioned earlier. During lithiation, the breaking of covalent Si–Si bonds allows Li atoms to saturate the resulting dangling bonds on the Si atoms.[47] The Si–Li bonds that form are anticipated to be mixed ionic-covalent or polar covalent in character, owing to the significant electronegativity difference between Si (1.90) and Li (0.98).[47,53] Although the presence of metals on Si, likely through local surface interactions as opposed to pure alloys not observed in the XRD data, could also affect the formation energy of Li_xSi, it requires a more in-depth first-principles analysis to demonstrate the energetics of SiM lithiation. We believe that the presence of metals can favorably alter this energetics, potentially leading to an overall reduction in overpotential.

EIS measurements of baseline Si, Si^{Ni}, and Si^{Al} half cells taken at various lithiation and delithiation potentials are shown in Fig. 9. A resistive (~110–150 Ω) interphase initially forms on all materials upon reaching 100 mV, then the interphase becomes less resistive (~50 Ω to 70 Ω) at 50 mV. Comparing the Nyquist plots at 100 mV for the metal-decorated materials with the baseline Si reveals two apparent

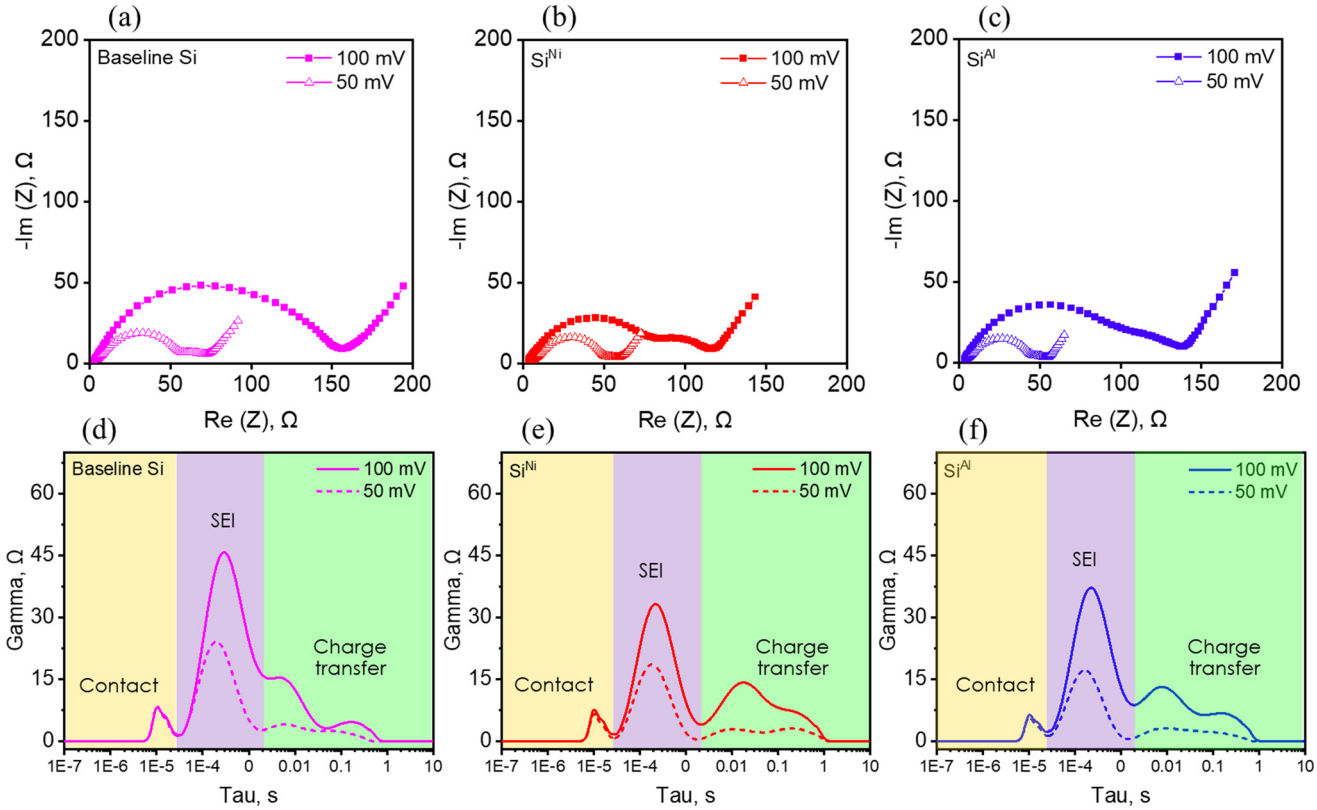

Fig. 9 Electrochemical impedance spectroscopy (EIS) Nyquist profiles at different lithiation potentials of a) baseline Si, b) Si^{Ni}, c) Si^{Al}, and the corresponding distribution of relaxation times (DRT) plots of d) baseline Si, e) Si^{Ni}, and f) Si^{Ni} within the 1 kHz to ~1 Hz frequency regime.

semicircles for Si^{Ni} and Si^{Al}, whereas the baseline Si only shows one distinct semicircle. Furthermore, these anodes exhibit smaller overall impedance compared to the baseline material at both lithiation potentials of 100 mV and 50 mV. For Si^{Ni}, this correlates with the superior cycle rate performance presented in Fig. 7.

Generally, cell impedance is influenced by various factors, including the choice of electrode materials, the electrolyte, and electrical connections within the cell.[54] The presence of specific metals, such as Ni, can reduce impedance, likely by enhancing electrical contacts, as indicated by the SSRM results. We employed the distribution of relaxation times (DRT) technique to gain model-free insights into the contributions of SEI and charge transfer processes on the observed impedance profiles between the high to mid-frequency regime (1 kHz to ~1 Hz).[55–60] This approach transforms the impedance data, which are a function of frequency, into a distribution of time constants. Here, the intensity of the peaks is related to resistance, while the peak positions can be associated with processes that take place at characteristic time constants, which can be used to compare dynamics and assign type of process occurring.

The resulting DRT plots in Fig. 9d–f reveal four apparent peaks for all examined materials. For instance, the Nyquist plot for the baseline material at 100 mV only shows one semicircle but clearly has the same number of peaks as the metal-decorated Si in the DRT plots. We tentatively assign the peaks $<10^{-4}$ s to contact resistance, the peaks at $\sim 10^{-4} < \tau < 10^{-2}$ s to SEI resistance, and $10^{-2} < \tau < 10$ s to charge transfer processes.[59] It is evident that the contact resistance (yellow region in Fig. 9d–f), is not significantly affected by the nature nor the state of charge of Si. The SEI (purple region in Fig. 9d–f) and charge transfer (green region in Fig. 9d–f) resistance are both lowered by the presence of metals on the Si surface. There are two features present in the charge transfer region for all anodes investigated. Based on the composition of the cells and the electrodes, Li–Si, Li-carbon black, and Li-P84 binder interactions[29,61–63] can all contribute to the observed peaks. On the other hand, only one peak is observed for the SEI and that the metals seem to influence the SEI response more than the charge transfer processes, which is important given that the SEI appears to dominate the overall Si cell impedance. Qualitatively, the resistance of the cells significantly decreased upon reaching 50 mV, with SiM maintaining a lower resistance, although not as significantly as at 100 mV over the bare Si. Overall, we note that metals can assist in the lithiation of Si electrodes by lowering the overall cell impedance.

DRT was further utilized to qualitatively analyze the delithiation process. As shown in Fig. S6,† the cell resistance decreases from the lithiated state until reaching 450 mV during delithiation for all materials. Beyond this point, the resistance increases upon continued delithiation to 750 mV and 1 V. Regardless of the cutoff potential, the resistance in

the delithiated states is lower than in the lithiated states for all materials, indicating the formation of less resistive interphases during delithiation. Additionally, the metal-decorated Si^{Ni} exhibits lower overall resistance after reaching the final delithiation potential of 1 V. These results suggest that for Si^{Ni}, the presence of metal helps minimize cell impedance during both lithiation and delithiation. Conversely, for Si^{Al}, the electrode appears to encounter detrimental processes during delithiation beyond 450 mV, as evidenced by a sudden increase in resistance, which exceeds that of the baseline Si at 750 mV and continues to rise until the final delithiation step at 1 V.

DRT plots were also derived from long-term cycling at C/3 and are summarized in Fig. S6.† Interestingly, the materials under investigation exhibit almost similar impedance peaks in the DRT upon continued cycling up to the 60th delithiation. However, a steady increase in SEI and charge transfer resistance is observed in baseline Si. In the case of Si^{Ni}, the SEI contribution remains unchanged during cycling, but the charge transfer resistance steadily increases from the 20th to the 60th delithiation. Notably, for Si^{Al}, the SEI contribution decreases during cycling, while the charge transfer resistance increases. Overall, the DRT profiles at delithiated states during formation and cycling suggest that the presence of metals indeed influences the SEI and charge transfer processes, thereby affecting the electrochemical performance of the electrodes. We propose that the presence of metals on the Si surface changes the energy barrier for Li desolvation, consequently affecting Li^+ transport kinetics and the processes at the interface.[64]

Select electrodes, specifically the baseline Si, Si^{Ni}, and Si^{Al}, were analyzed using XPS to examine the evolution of SEI composition at various stages of lithiation (250 mV, 100 mV, 50 mV) and delithiation (300 mV, 450 mV, 750 mV, and 1.5 V). Firstly, it appears from Fig. 10 the metal-decorated systems form a thicker SEI compared to the baseline Si. This is based on the Si signal visible for the baseline Si during the three lithiation potentials and until delithiation to 300 mV. In contrast, the Si signals for Si^{Ni} and Si^{Al} are visible during lithiation down to 100 mV, and the electrodes are completely covered in SEI once a potential of 50 mV is reached and throughout delithiation form 300 mV to 1.5 V. These data indicate that the metals promote a SEI that is thicker or less soluble than on the baseline Si resulting in Si XPS signal attenuation.

Furthermore, it seems the baseline (non-decorated) material forms more LiF products upon initial lithiation to 250 mV, whereas the metal-decorated Si^{Ni} and Si^{Al} show slightly lower LiF content. This is based on the surface concentration (at%) of Li and F, equivalent to 25.9 at% (Li) and 28.9 at% (F), and 24.3 at% (Li) and 30.8 at% (F) for Si^{Ni} and Si^{Al}, respectively, compared to 38.5 at% (Li) and 29. 2 at%(F) for the baseline Si. Upon further lithiation to 100 mV, the Li and F content in the metal-decorated electrodes increases to 31.6 at% (Li) and 35.5 at% (F) and 37.1 at% (Li) and 38.7 at% (F) for Si^{Ni} and Si^{Al}, respectively. For the baseline Si, Li content decreased to 32.8 at% and while the F content increased to 35.2 at%. During final lithiation down to 50 mV, the LiF in the baseline Si continues to increase slightly, while in Si^{Ni} it decreases, indicating a shift to more organic species based on the C and O content, at least at the top 5–10 nm of the electrode surface. Additionally, Si^{Al} either shows a slight decrease or remains constant in LiF content. Overall, Si^{Ni} has significantly less LiF at high states of charge and clearly has more C–O polymeric species, indicating either more polymerization or that the inorganic LiF is masked by the polymers. During the delithiation process, the metal-decorated electrodes, especially Si^{Al}, continue to develop more C- and O-containing species in the SEI, whereas the organic species in the baseline material only begin to increase significantly at 750 mV and 1.5 V. For Si^{Ni}, it appears that the formed SEI at the final state of charge maintains its overall composition upon delithiation. The elemental surface composition of the materials is summarized in Tables S5–S7.† Generally, it appears that the presence of metals on Si facilitate electrolyte decomposition, at least during the first cycle, to form a thicker SEI. Additionally, Ni seems to promote the formation of more organic species in the SEI, relative to the baseline Si. It appears that the formation of this thicker, insoluble SEI during initial cycling imparts

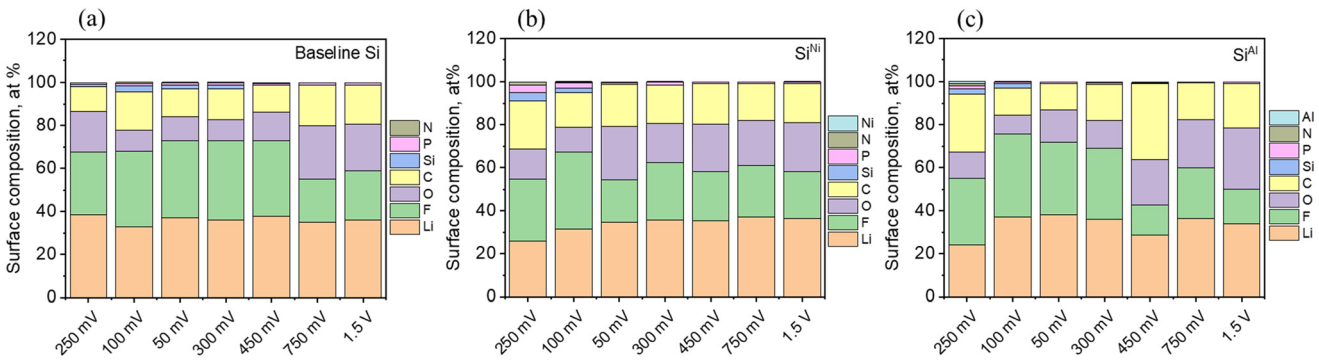

Fig. 10 Surface composition (at%) during lithiation at 250 mV, 100 mV, and 50 mV and *delithiation at 300 mV, 450 mV, 750 mV, and 1.5 V of the a) baseline Si, b) Si^{Ni}, and c) Si^{Al} in half-cells. *The electrodes were lithiated to 50 mV before delithiation.

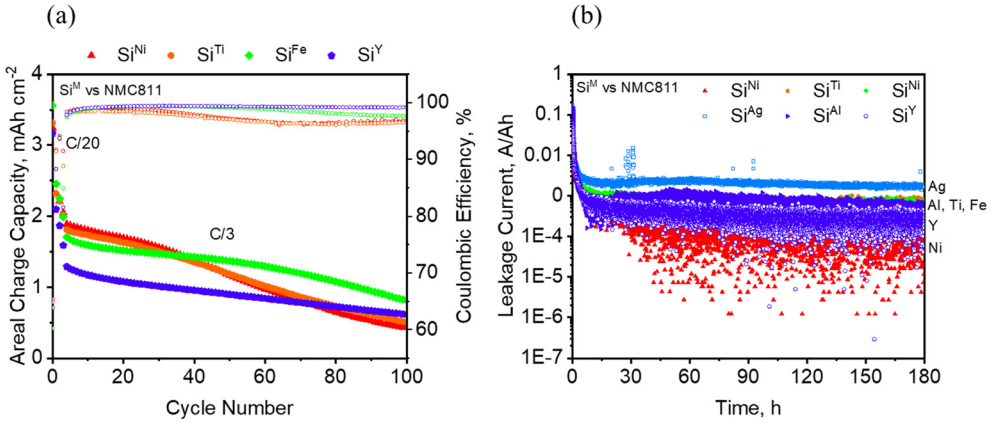

Fig. 11 a) Full cell cycling behavior of selected Si^{M} with NMC811 at a C/3 rate and b) leakage current of Si^{M} *vs.* NMC811 during charge at 4.1 V.

stability at the electrode/electrolyte interface, which may benefit subsequent cycling.

The performance of non-prelithiated Si^{M} electrodes, specifically Si^{Ni}, Si^{Ti}, Si^{Fe}, and Si^{Y} paired with a 3.07 mAh cm^{-2} cathode is illustrated in Fig. 11a. Si^{Ni} and Si^{Ti} show a steep decline in capacity at around 40 cycles, while Si^{Fe} also shows a fast decline near 60 cycles. In contrast, Si^{Y} demonstrates improved capacity retention, maintaining approximately 48% from the 5th to the 100th cycle. However, Si^{Ni}, Si^{Ti}, and Si^{Fe} initially exhibit higher capacities than Si^{Y}. For instance, the average areal capacities from the 5th to the 40th cycle are 1.63 mAh cm^{-2} for Si^{Ni}, 1.57 mAh cm^{-2} for Si^{Ti}, 1.51 mAh cm^{-2} for Si^{Fe}, and 1.07 mAh cm^{-2} for Si^{Y}. The sudden loss in capacity of Si^{Ni} and Si^{Ti} after approximately 40 cycles could be a consequence of deeper Si utilization, which could either exert greater stress on the materials or deplete more Li inventory from the cathode.

The full cell performance of Si^{Al} and Si^{Ag}, paired with different cathode loadings, is shown in Fig. S7.† For the 2.59 mAh cm^{-2} cell in Fig. S7a,† Si^{Ni} demonstrates an average of 0.5 Ah cm^{-2} higher areal capacity compared to Si^{Ag} over the course of 100 cycles. For the 4 mAh cm^{-2} cell presented in Fig. S7b,† Si^{Ti} and Si^{Fe} exhibit higher areal capacities than Si^{Al}, although Si^{Ti} and Si^{Fe} start to fade rapidly after about 30 cycles. Specifically, Si^{Ti} has 0.5 mAh cm^{-2} more capacity than Si^{Al}, while Si^{Fe} has 0.3 mAh cm^{-2} more capacity than Si^{Al} before exhibiting rapid capacity fade. Conversely, Si^{Al} displays a more gradual capacity fade over time, retaining approximately 44% of its capacity from the 5th cycle to the 100th cycle. Overall, this trend in areal capacities aligns with the half-cell performance depicted in Fig. 7 and 8. Moreover, it appears that the capacity fade observed in full cells particularly for the materials in which there is more capacity utilization, are exacerbated at higher electrode loadings. Finally, the admetals may be susceptible to crosstalk phenomena. The Si electrodes are known to promote the degradation of $LiPF_6$ electrolytes to form HF which may promote dissolution and reprecipitation on the cathode causing capacity losses.[65–67] These crosstalk processes result in the differences observed between the half and full cell experiments.

From Fig. 11b which shows the leakage current measured over a period of 180 hours during charged state in a full cell, it appears that the addition of Ni onto Si is beneficial in reducing the parasitic currents in the cell. This may be linked to the SEI composition obtained from XPS which seem to indicate that the formation of more organic components relative to the non-decorated Si, at least at the top 5–10 nm from the surface and during the formation cycle, leads to a more stable SEI, *i.e.* lower parasitic currents. On the other hand, the addition of Ag seems to increase the leakage current quite significantly. Since the measurements were conducted after three formation steps, it is reasonable to link the leakage current to the stability of the SEI formed on the electrodes. While this experiment may not definitively determine the cyclability of the electrodes, SEI stability likely impacts the calendar life of Si, which is an aspect that needs to be studied more. Nonetheless, Si^{Ni} demonstrated superior cycling performance compared to Si^{Ag}, and the overall observations across the different electrochemical experiments appear to agree with one another. The observed capacity fade in the full cell could be addressed through the use of a solid electrolyte to prevent crosstalk or limiting the extent of lithiation to avoid degradation of the silicon due to volume expansion effects.

Conclusions

In summary, this study showcased the preparation of metal-decorated Si powders, Si^{M}, as anode materials through a facile high energy ball milling process. Si^{Ni}, Si^{Fe}, and Si^{Ti} emerged as the best-performing materials, reducing the overpotential in half cells by up to 20 mV, improving the rate capability by a few hundred mAh g^{-1} compared to the baseline Si, and maintaining specific capacities greater than 1000 mAh g^{-1} beyond the 20th cycle, although with gradual fading. In contrast, Si^{Ag}, Si^{Al}, and Si^{Y} experienced significant capacity loss immediately after the formation steps. Electrode resistance measurements from SSRM correlated well with the cycling performance observed in half-cells. For instance, Si^{Ni} and Si^{Fe}, which exhibited overall lower electrode resistance

(8.7 logΩ and 9.4 logΩ), achieved higher specific capacities compared to Si^{Al}, which had higher electrode resistance (10.9 logΩ). This was further supported by differential capacity curves, where Si^{Al} showed an increase in overpotential with cycling, while Si^{Fe} exhibited minimal shifting in lithiation and delithiation potential with cycling. XPS studies revealed that Ni decoration promotes the formation of a thicker insoluble SEI, suggesting more extensive polymerization or salt decomposition, compared to the non-decorated Si. Moreover, the oxidation state of the metals as well as the zeta potential of the particles were also found to play a role. For example, the absence of oxidation in Ni can be associated with lower electrode resistance and improved performance. Finally, full-cell results were consistent with those from half-cells, with Si^{Ni}, Si^{Ti}, and Si^{Fe} displaying higher areal capacities but experiencing faster capacity fade, likely due to deeper Si utilization, particularly at higher electrode loadings.

Data availability

Data in this manuscript is X-Y type data and is maintained by the Oak Ridge National Laboratory as part of the electronic laboratory notebook program. For copies of this data contact Gabriel Veith (custodian) and they will be shared following ORNLs data management plan. There were no crystallographic databases, computer codes, or use of publicly available databases.

Conflicts of interest

The authors declare that they have no known competing financial interests or personal relationships that could have appeared to influence the work reported in this paper.

Acknowledgements

This research was supported by U.S. Department of Energy, Vehicle Technologies Office (DOE-VTO) under the Silicon Consortium Project, directed by Nicolas Eidson, Carine Steinway, Thomas Do, and Brian Cunningham, and managed by Anthony Burrell. This manuscript has been authored in part by UT-Battelle, LLC, under contract DE-AC05–00OR22725 with the US Department of Energy (DOE). The publisher, by accepting the article for publication, acknowledges that the US government retains a nonexclusive, paid-up, irrevocable, worldwide license to publish or reproduce the published form of this manuscript, or allow others to do so, for US government purposes. DOE will provide public access to these results of federally sponsored research in accordance with the DOE Public Access Plan (**https://energy.gov/downloads/doepublic-accessplan**). The STEM characterization work was conducted in the William R. Wiley Environmental Molecular Sciences Laboratory (EMSL), a national scientific user facility sponsored by DOE's Office of Biological and Environmental Research and located at PNNL. PNNL is operated by Battelle for the U.S. DOE under Contract DE-AC05-76RL01830. Argonne National Laboratory ("Argonne") is operated by UChicago Argonne LLC, and is a U.S. Department of Energy Office of Science laboratory, operated under Contract No. DE-AC02 – 06CH11357. National Renewable Energy Laboratory, operated by Alliance for Sustainable Energy, LLC, for the U. S. Department of Energy (DOE) under Contract No. DE-AC36-08GO28308.

References

1 B. L. Ellis and L. F. Nazar, Sodium and Sodium-Ion Energy Storage Batteries, *Curr. Opin. Solid State Mater. Sci.*, 2012, **16**(4), 168–177, DOI: **10.1016/j.cossms.2012.04.002**.

2 C. Delmas, Sodium and Sodium-Ion Batteries: 50 Years of Research, *Adv. Energy Mater.*, 2018, **8**(17), 1–9, DOI: **10.1002/aenm.201703137**.

3 P. Adelhelm, P. Hartmann, C. L. Bender, M. Busche, C. Eufinger and J. Janek, From Lithium to Sodium: Cell Chemistry of Room Temperature Sodium-Air and Sodium-Sulfur Batteries, *Beilstein J. Nanotechnol.*, 2015, **6**(1), 1016–1055, DOI: **10.3762/bjnano.6.105**.

4 S. Xie, W. Xie, Q. Zhang, X. Cheng, X. Ouyang and B. Lu, Structure-Engineered Low-Cost Carbon Microbelt Hosts for Highly Robust Potassium Metal Anode, *Adv. Funct. Mater.*, 2023, **33**(36), 1–11, DOI: **10.1002/adfm.202302880**.

5 A. Eftekhari, Z. Jian and X. Ji, Potassium Secondary Batteries, *ACS Appl. Mater. Interfaces*, 2017, **9**(5), 4404–4419, DOI: **10.1021/acsami.6b07989**.

6 J. Y. Hwang, S. T. Myung and Y. K. Sun, Recent Progress in Rechargeable Potassium Batteries, *Adv. Funct. Mater.*, 2018, **28**(43), 1–45, DOI: **10.1002/adfm.201802938**.

7 D. Chen, X. Mei, G. Ji, M. Lu, J. Xie, J. Lu and J. Y. Lee, Reversible Lithium-Ion Storage in Silver-Treated Nanoscale Hollow Porous Silicon Particles, *Angew. Chem., Int. Ed.*, 2012, **51**(10), 2409–2413, DOI: **10.1002/anie.201107885**.

8 J. W. Kim, J. H. Ryu, K. T. Lee and S. M. Oh, Improvement of Silicon Powder Negative Electrodes by Copper Electroless Deposition for Lithium Secondary Batteries, *J. Power Sources*, 2005, **147**(1–2), 227–233, DOI: **10.1016/j.jpowsour.2004.12.041**.

9 S. Yoo, J. I. Lee, S. Ko and S. Park, Highly Dispersive and Electrically Conductive Silver-Coated Si Anodes Synthesized via a Simple Chemical Reduction Process, *Nano Energy*, 2013, **2**(6), 1271–1278, DOI: **10.1016/j.nanoen.2013.06.006**.

10 Y. Yu, L. Gu, C. Zhu, S. Tsukimoto, P. A. Van Aken and J. Maier, Reversible Storage of Lithium in Silver-Coated Three-Dimensional Macroporous Silicon, *Adv. Mater.*, 2010, **22**(20), 2247–2250, DOI: **10.1002/adma.200903755**.

11 H. Zhang, S. Liu, X. Yu and S. Chen, Improving Rate Capacity and Cycling Stability of Si-Anode Lithium Ion Battery by Using Copper Nanowire as Conductive Additive, *J. Alloys Compd.*, 2020, **822**, 153664, DOI: **10.1016/j.jallcom.2020.153664**.

12 D.-H. Lee, H.-W. Shim and D.-W. Kim, Facile Synthesis of Heterogeneous Ni-Si@C Nanocomposites as High-Performance Anodes for Li-Ion Batteries, *Electrochim. Acta*, 2014, **146**, 60–67, DOI: **10.1016/j.electacta.2014.08.103**.

13 J. Liang, Y. Yang, J. Gao, L. Zhou, M. Gao, Z. Zhang, W. Yang, M. Javid, Y. Jung, X. Dong and G. Cao, Morphological and Structural Evolution of Si-Cu Nanocomposites by an Instantaneous Vapor-Liquid-Solid Growth and the Electrochemical Lithiation/Delithiation Performances, *J. Solid State Electrochem.*, 2019, **23**(3), 735–748, DOI: **10.1007/s10008-018-04173-6**.

14 S. Murugesan, J. T. Harris, B. A. Korgel and K. J. Stevenson, Copper-Coated Amorphous Silicon Particles as an Anode Material for Lithium-Ion Batteries, *Chem. Mater.*, 2012, **24**(7), 1306–1315, DOI: **10.1021/cm2037475**.

15 A. Paravannoor, D. Panoth and P. Pattathil, Silicon Anode Design for Li Ion Batteries: Synergic Effects of Ag Nanoparticles and Ionic Liquid Electrolytes, *Chem. Eng. J. Adv.*, 2020, **4**, 100037, DOI: **10.1016/j.ceja.2020.100037**.

16 B. D. Polat and O. Keles, Improving Si Anode Performance by Forming Copper Capped Copper-Silicon Thin Film Anodes for Rechargeable Lithium Ion Batteries, *Electrochim. Acta*, 2015, **170**, 63–71, DOI: **10.1016/j.electacta.2015.04.131**.

17 V. A. Sethuraman, K. Kowolik and V. Srinivasan, Increased Cycling Efficiency and Rate Capability of Copper-Coated Silicon Anodes in Lithium-Ion Batteries, *J. Power Sources*, 2011, **196**(1), 393–398, DOI: **10.1016/j.jpowsour.2010.06.043**.

18 F. Wang, S. Xu, S. Zhu, H. Peng, R. Huang, L. Wang, X. Xie and P. K. Chu, Ni-Coated Si Microchannel Plate Electrodes in Three-Dimensional Lithium-Ion Battery Anodes, *Electrochim. Acta*, 2013, **87**, 250–255, DOI: **10.1016/j.electacta.2012.09.122**.

19 X. Yang, Z. Wen, S. Huang, X. Zhu and X. Zhang, Electrochemical Performances of Silicon Electrode with Silver Additives, *Solid State Ionics*, 2006, **177**(26–32 SPEC. ISS), 2807–2810, DOI: **10.1016/j.ssi.2006.03.033**.

20 S. Yin, Q. Ji, X. Zuo, S. Xie, K. Fang, Y. Xia, J. Li, B. Qiu, M. Wang, J. Ban, X. Wang, Y. Zhang, Y. Xiao, L. Zheng, S. Liang, Z. Liu, C. Wang and Y.-J. Cheng, Silicon Lithium-Ion Battery Anode with Enhanced Performance: Multiple Effects of Silver Nanoparticles, *J. Mater. Sci. Technol.*, 2018, **34**(10), 1902–1911, DOI: **10.1016/j.jmst.2018.02.004**.

21 Q. Zhang, L. Wang, J. Wang, X. Yu, J. Ge, H. Zhang and B. Lu, Semimetallic Vanadium Molybdenum Sulfide for High-Performance Battery Electrodes, *J. Mater. Chem. A*, 2018, **6**(20), 9411–9419, DOI: **10.1039/c8ta00995c**.

22 J. H. Ryu, J. W. Kim, Y.-E. Sung and S. M. Oh, Failure Modes of Silicon Powder Negative Electrode in Lithium Secondary Batteries, *Electrochem. Solid-State Lett.*, 2004, **7**(10), A306, DOI: **10.1149/1.1792242**.

23 K. Guo, Q. Pan, L. Wang and S. Fang, Nano-Scale Copper-Coated Graphite as Anode Material for Lithium-Ion Batteries, *J. Appl. Electrochem.*, 2002, **32**(6), 679–685, DOI: **10.1023/A:1020178121795**.

24 I. Sandu, T. Brousse and D. M. Schleich, Effect of Nickel Coating on Electrochemical Performance of Graphite Anodes for Lithium Ion Batteries, *Ionics*, 2003, **9**(5–6), 329–335, DOI: **10.1007/BF02376582**.

25 J. Yun, Y. Wang, T. Gao, H. Zheng, M. Shen, Q. Qu and H. Zheng, In-Situ Electrochemical Coating of Ag Nanoparticles onto Graphite Electrode with Enhanced Performance for Li-Ion Batteries, *Electrochim. Acta*, 2015, **155**, 396–401, DOI: **10.1016/j.electacta.2014.12.129**.

26 L. J. Fu, J. Gao, T. Zhang, Q. Cao, L. C. Yang, Y. P. Wu and R. Holze, Effect of Cu2O Coating on Graphite as Anode Material of Lithium Ion Battery in PC-Based Electrolyte, *J. Power Sources*, 2007, **171**(2), 904–907, DOI: **10.1016/j.jpowsour.2007.05.099**.

27 K. G. Arano, B. L. Armstrong, A. W. Tomich, M. S. Chambers, J. Quinn, H. M. Meyer III, C. Kumara, Z. Huey, C.-S. Jiang, C. Wang, C. S. Johnson and G. M. Veith, Investigating the Impact of Preparation Routes on the Properties of Copper-Decorated Si Particles as Anode Materials for Lithium-Ion Batteries, submitted.

28 K. G. Araño, B. L. Armstrong, G. Yang, C. Kumara, T. Z. Ward, H. M. Meyer, A. M. Rogers, E. Toups and G. M. Veith, Elucidating the Role of Carbon Conductive Additive in the Processing and Electrochemical Behavior of Surface-Modified Si Anodes, *Energy Fuels*, 2024, **38**(7), 6446–6458, DOI: **10.1021/acs.energyfuels.4c00039**.

29 K. G. Araño, B. L. Armstrong, E. Boeding, G. Yang, H. M. Meyer, E. Wang, R. Korkosz, K. L. Browning, T. Malkowski, B. Key and G. M. Veith, Functionalized Silicon Particles for Enhanced Half- and Full-Cell Cycling of Si-Based Li-Ion Batteries, *ACS Appl. Mater. Interfaces*, 2023, **15**(8), 10554–10569, DOI: **10.1021/acsami.2c16978**.

30 K. G. Araño, G. Yang, B. L. Armstrong, T. Aytug, M. S. Chambers, E. C. Self, H. M. Meyer, J. Quinn, J. F. Browning, C. Wang and G. M. Veith, Carbon Coating Influence on the Formation of Percolating Electrode Networks for Silicon Anodes, *ACS Appl. Energy Mater.*, 2023, **6**(21), 11308–11321, DOI: **10.1021/acsaem.3c02205**.

31 H. M. Rietveld, A Profile Refinement Method for Nuclear and Magnetic Structures, *J. Appl. Crystallogr.*, 1969, **2**(2), 65–71, DOI: **10.1107/S0021889869006558**.

32 A. A. Coelho, J. Evans, I. Evans, A. Kern and S. Parsons, The TOPAS Symbolic Computation System, *Powder Diffr.*, 2011, **26**(S1), S22–S25, DOI: **10.1154/1.3661087**.

33 D. Balzar, N. Audebrand, M. R. Daymond, A. Fitch, A. Hewat, J. I. Langford, A. Le Bail, D. Louër, O. Masson, C. N. McCowan, N. C. Popa, P. W. Stephens and B. H. Toby, Size-Strain Line-Broadening Analysis of the Ceria Round-Robin Sample, *J. Appl. Crystallogr.*, 2004, **37**(6), 911–924, DOI: **10.1107/S0021889804022551**.

34 P. Eyben, M. Xu, N. Duhayon, T. Clarysse, S. Callewaert and W. Vandervorst, Scanning Spreading Resistance Microscopy and Spectroscopy for Routine and Quantitative Two-Dimensional Carrier Profiling, *J. Vac. Sci. Technol., B: Microelectron. Nanometer Struct.–Process., Meas., Phenom.*, 2002, **20**(1), 471–478, DOI: **10.1116/1.1424280**.

35 P. Eyben, F. Clemente, K. Vanstreels, G. Pourtois, T. Clarysse, E. Duriau, T. Hantschel, K. Sankaran, J. Mody, W. Vandervorst, K. Mylvaganam and L. Zhang, Analysis and Modeling of the High Vacuum Scanning Spreading Resistance Microscopy Nanocontact on Silicon, *J. Vac. Sci. Technol., B*, 2010, **28**(2), 401–406, DOI: **10.1116/1.3273895**.

36 T. H. Wan, M. Saccoccio, C. Chen and F. Ciucci, Influence of the Discretization Methods on the Distribution of Relaxation Times Deconvolution: Implementing Radial Basis Functions with DRTtools, *Electrochim. Acta*, 2015, **184**, 483–499, DOI: **10.1016/j.electacta.2015.09.097**.
37 rhd instruments. RelaxIS DRT - Distribution of Relaxation Times. **https://relaxis-drt.rhd-instruments.de/**.
38 O. K. Goldbeck, *IRON—Binary Phase Diagrams*, Springer, Berlin, Heidelberg, 1982. DOI: **10.1007/978-3-662-08024-5**.
39 M. Shamsuzzoha and F. R. Juretzko, Dual Refinement of Primary and Eutectic Si in Hypereutectic Al-Si Alloys, *Aluminium Alloys for Transportation, Packaging, Aerospace, and Other Applications*, ed. S. K. Das and W. Yin, 2007.
40 S. Sabooni, F. Karimzadeh and M. H. Abbasi, Thermodynamic Aspects of Nanostructured Ti5Si3 Formation During Mechanical Alloying and Its Characterization, *Bull. Mater. Sci.*, 2012, **35**(3), 439–447, DOI: **10.1007/s12034-012-0298-2**.
41 A. B. Gokhale and G. J. Abbaschian, The Si–Y (Silicon-Yttrium) System, *Bull. Alloy Phase Diagrams*, 1986, **7**(5), 485–489, DOI: **10.1007/BF02867814**.
42 K. van Stiphout, A. Vantomme and K. Temst, Metastability in Nickel Silicide and Nickel Germanide Thin Film Reactions, *PhD Thesis*, KU Leuven, 2018.
43 R. W. Olesinski, A. B. Gokhale and G. J. Abbaschian, The Ag-Si (Silver-Silicon) System, *Bull. Alloy Phase Diagrams*, 1989, **10**(6), 635–640, DOI: **10.1007/BF02877631**.
44 W. A. Appiah, L. H. Rieger, E. Flores, T. Vegge and A. Bhowmik, Unravelling Degradation Mechanisms and Overpotential Sources in Aged and Non-Aged Batteries: A Non-Invasive Diagnosis, *J. Energy Storage*, 2024, **84**, 111000, DOI: **10.1016/j.est.2024.111000**.
45 Z. Chen, D. L. Danilov, L. H. J. Raijmakers, K. Chayambuka, M. Jiang, L. Zhou, J. Zhou, R.-A. Eichel and P. H. L. Notten, Overpotential Analysis of Graphite-Based Li-Ion Batteries Seen from a Porous Electrode Modeling Perspective, *J. Power Sources*, 2021, **509**, 230345, DOI: **10.1016/j.jpowsour.2021.230345**.
46 L. Luo, J. Wu, J. Luo, J. Huang and V. P. Dravid, Dynamics of Electrochemical Lithiation/Delithiation of Graphene-Encapsulated Silicon Nanoparticles Studied by In-Situ TEM, *Sci. Rep.*, 2014, **4**(1), 3863, DOI: **10.1038/srep03863**.
47 K. Zhao, W. L. Wang, J. Gregoire, M. Pharr, Z. Suo, J. J. Vlassak and E. Kaxiras, Lithium-Assisted Plastic Deformation of Silicon Electrodes in Lithium-Ion Batteries: A First-Principles Theoretical Study, *Nano Lett.*, 2011, **11**(7), 2962–2967, DOI: **10.1021/nl201501s**.
48 K. Mala, M. Wahid, S. W. Gosavi, S. I. Patil and S. M. Jejurikar, Investigating the Role of Crystallographic Orientation of Single Crystalline Silicon on Their Electrochemical Lithiation Behavior: Surface Chemistry of Si Determines the Bulk Lithiation, *Surf. Interfaces*, 2020, **20**, 100585, DOI: **10.1016/j.surfin.2020.100585**.
49 V. L. Chevrier, J. W. Zwanziger and J. R. Dahn, First Principles Study of Li–Si Crystalline Phases: Charge Transfer, Electronic Structure, and Lattice Vibrations, *J. Alloys Compd.*, 2010, **496**(1), 25–36, DOI: **10.1016/j.jallcom.2010.01.142**.
50 Y. Wang and J. R. Dahn, Comparison of the Reactions Between Lix Si or Li0.81C6 and Nonaqueous Solvent or Electrolytes at Elevated Temperature, *J. Electrochem. Soc.*, 2006, **153**(12), A2188, DOI: **10.1149/1.2354458**.
51 M. N. Obrovac and L. J. Krause, Reversible Cycling of Crystalline Silicon Powder, *J. Electrochem. Soc.*, 2007, **154**(2), A103–A108, DOI: **10.1149/1.2402112**.
52 J. Brizuela, M. V. Bracamonte, D. E. Barraco and M. Otero, First Principles Investigation of LixSi and LixSn Alloys: Unraveling Atomic-Scale Influences on Material Properties, *J. Power Sources*, 2024, **609**, 234657, DOI: **10.1016/j.jpowsour.2024.234657**.
53 H. Kim, K. E. Kweon, C.-Y. Chou, J. G. Ekerdt and G. S. Hwang, On the Nature and Behavior of Li Atoms in Si: A First Principles Study, *J. Phys. Chem. C*, 2010, **114**(41), 17942–17946, DOI: **10.1021/jp104289x**.
54 K. W. Beard, *Linden's Handbook of Batteries*, McGraw Hill LLC, 5th edn. 2019.
55 J. P. Schmidt, P. Berg, M. Schönleber, A. Weber and E. Ivers-Tiffée, The Distribution of Relaxation Times as Basis for Generalized Time-Domain Models for Li-Ion Batteries, *J. Power Sources*, 2013, **221**, 70–77, DOI: **10.1016/j.jpowsour.2012.07.100**.
56 S. Gantenbein, M. Weiss and E. Ivers-Tiffée, Impedance Based Time-Domain Modeling of Lithium-Ion Batteries: Part I, *J. Power Sources*, 2018, **379**, 317–327, DOI: **10.1016/j.jpowsour.2018.01.043**.
57 X. Zhou, J. Huang, Z. Pan and M. Ouyang, Impedance Characterization of Lithium-Ion Batteries Aging under High-Temperature Cycling: Importance of Electrolyte-Phase Diffusion, *J. Power Sources*, 2019, **426**, 216–222, DOI: **10.1016/j.jpowsour.2019.04.040**.
58 X. Chen, L. Li, M. Liu, T. Huang and A. Yu, Detection of Lithium Plating in Lithium-Ion Batteries by Distribution of Relaxation Times, *J. Power Sources*, 2021, **496**, 229867, DOI: **10.1016/j.jpowsour.2021.229867**.
59 P. Iurilli, C. Brivio and V. Wood, Detection of Lithium-Ion Cells' Degradation through Deconvolution of Electrochemical Impedance Spectroscopy with Distribution of Relaxation Time, *Energy Technol.*, 2022, **10**(10), 2200547, DOI: **10.1002/ente.202200547**.
60 R. Soni, J. B. Robinson, P. R. Shearing, D. J. L. Brett, A. J. E. Rettie and T. S. Miller, Lithium-Sulfur Battery Diagnostics Through Distribution of Relaxation Times Analysis, *Energy Storage Mater.*, 2022, **51**, 97–107, DOI: **10.1016/j.ensm.2022.06.016**.
61 N.-S. Choi, K. H. Yew, W.-U. Choi and S.-S. Kim, Enhanced Electrochemical Properties of a Si-Based Anode Using an Electrochemically Active Polyamide Imide Binder, *J. Power Sources*, 2008, **177**(2), 590–594, DOI: **10.1016/j.jpowsour.2007.11.082**.
62 T. Yoon, N. Chapman, C. C. Nguyen and B. L. Lucht, Electrochemical Reactivity of Polyimide and Feasibility as a Conductive Binder for Silicon Negative Electrodes, *J. Mater. Sci.*, 2017, **52**(7), 3613–3621, DOI: **10.1007/s10853-016-0442-2**.
63 J. Choi, K. Kim, J. Jeong, K. Y. Cho, M.-H. Ryou and Y. M. Lee, Highly Adhesive and Soluble Copolyimide Binder:

Improving the Long-Term Cycle Life of Silicon Anodes in Lithium-Ion Batteries, *ACS Appl. Mater. Interfaces*, 2015, **7**(27), 14851–14858, DOI: **10.1021/acsami.5b03364**.

64 S. Lei, Z. Zeng, M. Liu, H. Zhang, S. Cheng and J. Xie, Balanced Solvation/De-Solvation of Electrolyte Facilitates Li-Ion Intercalation for Fast Charging and Low-Temperature Li-Ion Batteries, *Nano Energy*, 2022, **98**, 107265, DOI: **10.1016/j.nanoen.2022.107265**.

65 S. G. Yoon, K. H. Lee and M. Kim, Transition metal crosstalk in conventional graphite-based batteries and advanced silicon-based batteries, *Appl. Phys. Lett.*, 2022, **121**, 200503, DOI: **10.1063/5.0116349**.

66 Y. Song, L. Wang, L. Sheng, D. Ren, H. Liang, Y. Li, A. Wang, H. Zhang, H. Xu and X. He, The significance of mitigating crosstalk in lithium-ion batteries: a review, *Energy Environ. Sci.*, 2023, **16**(5), 1943–1963, DOI: **10.1039/D3EE00441D**.

67 Y. Song, L. Wang, L. Sheng, M. Zhang, H. Liang, D. Ren, H. Cui, H. Zhang, H. Xu and X. He, The significance of imperceptible crosstalk in high-energy batteries, *Energy Storage Mater.*, 2023, **63**, 103018, DOI: **10.1016/j.ensm.2023.103018**.